Deep-inelastic neutron scattering from liquid ^{4}He

T. R. Sosnick* and W. M. Snow†
Intense Pulsed Neutron Source, Argonne National Laboratory, Argonne, Illinois 60439

P. E. Sokol
Department of Physics, The Pennsylvania State University, University Park, Pennsylvania 61802
(Received 20 November 1989)

Deep-inelastic neutron scattering measurements on liquid ^{4}He have been carried out for temperatures from 0.35 to 4.2 K at a density of 0.147 g/cm^3. These measurements have a relative resolution comparable to previous reactor measurements, but at a momentum transfer of 23 Å^{-1}. This momentum transfer is sufficiently high that the differences between the observed scattering and that predicted by the impulse approximation are small and are well described by a recent theoretical treatment allowing direct information on the single-particle momentum distribution to be obtained from the scattering measurements. The scattering in the normal liquid phase is broad and featureless with a nearly Gaussian shape. The scattering in the superfluid phase is distinctly non-Gaussian with extra intensity at the peak center consistent with the presence of a Bose condensate. However, no distinct peak due to the Bose condensate is observed even when the effects of instrumental broadening are included. When deviations from the impulse approximation are taken into account using a recent theory, the experimental results at 0.35 K are in excellent agreement with *ab initio* ground-state variational and Green's-function Monte Carlo calculations in the superfluid at $T=0$ K. The results at higher temperatures are in excellent agreement with recent path-integral Monte Carlo calculations in both the normal and superfluid phases. Fits of model functions to the scattering are also presented. The average kinetic energy per atom has been determined and is in good agreement with theoretical predictions and with previous experimental results.

I. INTRODUCTION

Liquid ^{4}He is one of the most intensively studied systems in the history of physics. The weak attractive forces between the atoms and their large zero-point motion combine to stabilize the liquid phase of helium under its saturated vapor pressure even at zero temperature. The effects of the Bose statistics of the helium atoms are important in the liquid, and at a sufficiently low temperature liquid ^{4}He undergoes a second-order phase transition to a superfluid phase. The efforts over many decades to understand the superfluidity of liquid ^{4}He have produced innovative ideas and techniques of broad significance in both theory and experiment. Today it enjoys a unique status as a model system for the study of several aspects of many-body physics. Ironically, it has attained this status despite the fact that a detailed microscopic theory of the liquid does not exist. A glance at the current state of our understanding of one of the simplest properties of liquid ^{4}He, its momentum distribution, will serve to bring this irony into focus.

Bose condensation provides the microscopic basis for our present theoretical understanding of superfluidity in bulk liquid ^{4}He.[1] According to this view, the superfluid phase is described by a macroscopic wave function

$$\langle\psi\rangle=\sqrt{n_0}\exp(i\phi)\ . \tag{1.1}$$

The square of the amplitude of $\langle\psi\rangle$ is the fraction of atoms in the condensate, and its phase is coherent on a macroscopic scale. The gradient of this phase is proportional to the superfluid velocity, the new hydrodynamic degree of freedom which appears in the well-known two-fluid model. Quantized vortices arise as a result of the quantization of superfluid circulation required by the single-valued nature of the macroscopic wave function. Even the phonon-maxon-roton spectrum of elementary excitations is an indirect consequence of the presence of a condensate.[2] None of these properties of superfluid ^{4}He, however, depends in detail on the exact magnitude of the condensate. Only its existence is necessary. In this way, many of the properties of the liquid which make it a model system are insulated from our ignorance of the condensate and the detailed microscopic physics which determine its size.

The momentum distribution $n(p)$ of superfluid ^{4}He, however, is different in this respect. In the absence of a detailed microscopic theory, the momentum distribution is the only measurable property of the liquid which can reveal the size of the condensate. It is this characteristic of the momentum distribution which makes its measurement an issue of fundamental interest. In a sample of liquid ^{4}He at rest, a condensate would produce a δ-function spike in the momentum distribution centered at $p=0$ with an intensity proportional to the fraction of atoms in the condensate, n_0.

Liquid helium is a dense, strongly interacting many-body system. Its momentum distribution is dominated by the effects of the strong short-range repulsion between the atoms and the high atomic density. Even at zero

temperature, these factors suffice to force the great majority of the atoms in superfluid ^{4}He out of the condensate. The kinetic energy of these atoms is almost entirely determined by the effects of atomic zero-point motion. As a result, the standard methods of many-body perturbation theory are doomed to failure in a calculation of the momentum distribution from first principles. (The only result derivable from standard many-body methods, assuming a condensate exists, is the existence of a weak power-law singularity in the momentum distribution at $p=0$ due to the zero-point motion of long-wavelength phonons.[3])

This absence of a detailed microscopic theory has inspired the development of many alternative approaches to the calculation of the momentum distribution in helium. The first realistic calculation of the momentum distribution of liquid ^{4}He at $T=0$ was a variational calculation[4] using a trial wave function of the Jastrow form, which is a product of pair functions. The parameters in the pair function were determined by the variational method, with the necessary configuration space integrals performed by Monte Carlo techniques. The helium-helium interactions were described by a Lennard-Jones potential. Gradual improvements were made in the implementation of the variational calculations, such as the proper inclusion of the effects of zero-point phonons, the use of the Aziz potential[5] in place of the Lennard-Jones potential, the development of hypernetted chain calculation methods, and the extension of the trial wave function to include three-body correlations.[6–17] In the most recent variational calculations,[18] the variational ground state includes the effects of two- and three-body correlations. The one-body density matrix, which is the Fourier transform of the momentum distribution, is then calculated in a cluster expansion using the hypernetted-chain scaling (HNC/S) approximation.

For the finite-temperature extensions of the variational calculations, the low-lying excited states are generated from the ground-state wave function used at zero temperature with an operator first proposed by Feynman and Cohen.[19] The change in the momentum distribution caused by the creation of a single excitation is calculated using the HNC/S method. At temperatures low enough that the interactions between elementary excitations can be neglected ($T<1$ K), the momentum distribution can be obtained by simply adding the induced changes to the ground-state momentum distribution weighted by the Bose distribution function.

An intrinsic limitation of the variational calculations is the fact that the proposed form of the wave function may not possess sufficient freedom to capture all of the important physical effects. This limitation is bypassed, in principle, in the Green's-function Monte Carlo method (GFMC).[20] In the GFMC method, which is restricted to zero temperature, a solution for the ground-state wave function is generated stochastically. The Schrödinger equation in imaginary time is converted into a diffusion equation in real time, which can be solved by Monte Carlo techniques. In practice, importance sampling may bias these results toward the sampling function.[21] However, in general, these results are believed to be quite accurate.

At finite temperatures above 1 K, the momentum distribution has been calculated using the path-integral Monte Carlo method (PIMC).[22] In the PIMC method, the starting point is an accurate representation of the density matrix at high temperature. The low-temperature density matrix can be expressed as a path integral over products of high-temperature density matrices.[23] The path integrals are performed using a generalization of the Metropolis Monte Carlo algorithm. A special feature of the PIMC calculation is its ability to calculate the momentum distribution in both the normal liquid phase and superfluid phases.

Over the past few years significant advances have been made in the sophistication of all of these methods. The results for many properties of liquid ^{4}He, such as the equation of state,[20] the static structure factor,[22] the elementary excitation spectrum,[24] and even the superfluid fraction[25] are in good agreement with each other and with experiment. On the basis of this agreement, the calculations of the momentum distribution are expected to be quite accurate. We will use the results of all of these methods in our comparisons with the neutron scattering data.

The most direct method for measuring the momentum distribution in liquid ^{4}He is through the use of deep-inelastic neutron scattering (DINS). For sufficiently high momentum transfers the dynamic structure factor describing the scattering of neutrons by the helium atoms, $S(Q,\omega)$, is directly related to $n(p)$ through the impulse approximation (IA).[26] This direct relation between $S_{\rm IA}(Q,\omega)$ and $n(p)$, coupled with the interest in the Bose condensate, has been a major source of inspiration for the numerous inelastic neutron scattering experiments performed on helium.

Most high-resolution measurements to data have been confined to the relatively low-Q (4–10 Å^{-1}) neutrons available at reactors. In the most recent of these studies,[27,28] a definite change in the scattering is observed upon entering the superfluid phase. Unfortunately, sizable deviations from the IA obscure the detailed features of the momentum distribution. Experiments at significantly larger $Q>50$ Å^{-1} have also been performed at spallation neutron sources.[29,30] However, in these measurements the instrumental resolution was comparable to the intrinsic width of the scattering, making the extraction of information on the momentum distribution difficult. Direct comparisons of past experimental results with the accurate calculations of $n(p)$ now available have shown large discrepancies.[15,18,31–33] Furthermore, it is important to realize that no distinct feature characteristic of the superfluid, like a narrow peak in $n(p)$ at $p=0$, has ever been observed in any of these experiments.

Even if the condensate exists, this failure to observe a sharp feature in the neutron scattering data is not surprising. At finite Q the IA is not valid, and sharp features which exist in the momentum distribution are significantly broadened. These broadening effects, due to the influence of the interactions among helium atoms on the final scattering state of the neutron, are known as final-state effects (FSE). As a result of FSE, the momentum distribution of the scattered neutrons is broader and

different in shape than the momentum distribution of the helium atoms from which they have scattered.

It is important to realize that final-state effects are not simply an uninteresting complication in the search for the condensate. FSE are of considerable interest in their own right, and an accurate calculation of their influence presents a challenging theoretical problem. The manner in which inelastic scattering approaches the IA limit can be crucial for the interpretation of a number of experiments in many areas of physics. For example, a quantitative understanding of FSE in inelastic neutron scattering from a relatively simple system such as liquid ^{4}He could be expected to lead to progress in the treatment of FSE in quasielastic electron-nucleus scattering.[34]

In this paper, we report new high-resolution neutron scattering studies of $S(Q,\omega)$ in liquid ^{4}He in both the normal and superfluid phases using much higher Q's than in previous high-resolution experiments. Using a recent theory for FSE which is applicable at the Q's used here, excellent agreement between experiment and the theoretical $n(p)$ is obtained in both the superfluid and normal liquid phases with no adjustable parameters. Our results provide strong evidence for a narrow component in the $n(p)$ of the superfluid phase that contains $\sim 9\%$ of the atoms, corresponding to the condensate.

This paper is organized as follows. Section II contains a discussion of inelastic neutron scattering. The relation of the scattering data to the longitudinal momentum distribution and the importance of final-state effects and the difficulties involved in extracting information on $n(p)$ from the observed scattering are emphasized. Section III covers experimental details. It contains a concise explanation of the operation of the PHOENIX spectrometer and our methods of data analysis with emphasis on the special features made possible by Y scaling. In Sec. IV our experimental results are compared to the theoretical momentum distributions broadened by instrumental resolution and final-state effects. In addition, we present fits of model functions to the observed scattering. These fits are then used to extract values for the average kinetic energy per atom. Finally, we end with our conclusions.

II. INELASTIC NEUTRON SCATTERING

Any superposition of single low-energy neutron-nucleus scattering events can be described, to an excellent approximation,[35] by the double-differential scattering cross section

$$\frac{d^2\sigma}{d\Omega\, d\omega} = b^2 \frac{k_f}{k_i} S(Q,\omega) , \tag{2.1}$$

where b is the scattering length, k_i and k_f are the initial and final wave vectors of the scattered neutron, and Q and ω are the momentum and energy transfer from the neutron to the sample. The dynamics of the sample are contained in $S(Q,\omega)$, the dynamic structure factor, which is directly proportional to the space and time Fourier transform of the density-density correlation function.[36]

The density fluctuations which contribute to $S(Q,\omega)$ include both collective excitations involving many atoms and single-particle excitations. For sufficiently large Q, the distance over which the phase of the incident neutron changes significantly during the scattering process, which is $\sim 2\pi/Q$, is small compared with the distance between the scattering atoms. The part of $S(Q,\omega)$ due to the interference of scattering amplitudes from different atoms becomes negligible due to phase cancellation, and the scattering is due primarily to single-particle excitations. In this limit, known as the incoherent approximation, the expression for $S(Q,\omega)$ becomes

$$S_{\rm inc}(Q,\omega) = \int_{-\infty}^{+\infty} \exp\left[-\frac{i\omega t}{\hbar}\right] \langle \exp[-i\mathbf{Q}\cdot\mathbf{r}(0)] \exp[-i\mathbf{Q}\cdot\mathbf{r}(t)] \rangle dt , \tag{2.2}$$

where $\mathbf{r}(t)$ is the position vector of an atom and $\langle \cdots \rangle$ signifies a thermodynamic average. The incoherent approximation for scattering from bulk helium should apply to liquid helium for $Q > 10$ Å^{-1}.[37] Measurements of the static structure factor $S(Q)$, which is related to the Fourier transform of the pair distribution function, indicate that static density correlations in liquid ^{4}He are quite small for $Q > 8$ Å^{-1}.[37] In our experiments, Q at the center of the recoil peak is 23 Å^{-1}, and the incoherent approximation is certainly applicable.

The frequency moments of $S_{\rm inc}(Q,\omega)$ provide valuable information on the energy dependence of the scattering function for fixed Q. In general, they depend explicitly on the details of the interactions between the atoms. However, the first three moments of $S_{\rm inc}(Q,\omega)$ are independent of these details.[38] These moments are

$$M_0(Q) = \int S_{\rm inc}(Q,\omega) d\omega = 1 , \tag{2.3}$$

$$M_1(Q) = \int (\omega - \omega_r) S_{\rm inc}(Q,\omega) d\omega = 0 , \tag{2.4}$$

$$M_2(Q) = \int (\omega - \omega_r)^2 S_{\rm inc}(Q,\omega) d\omega = \tfrac{4}{3}\omega_r \langle E_k \rangle , \tag{2.5}$$

where the recoil energy, ω_r, is $\hbar^2 Q^2/2M_{\rm He}$ and $M_{\rm He}$ is the mass of the scattering atom. Under the conditions of the incoherent approximation, the average kinetic energy per atom, $\langle E_k \rangle$, can be obtained directly from the second moment of the observed scattering.

At very high momentum transfers, the form for $S(Q,\omega)$ simplifies considerably from Eq. (2.2). In this limit, the impulse imparted to the target atom by the neutron during the collision far exceeds the impulse transferred by neighboring helium atoms and only single-particle properties are probed. The scattering can then be described by the well-known impulse approximation which directly relates $S(Q,\omega)$ to the atomic momentum distribution, $n(\mathbf{p})$

$$\lim_{Q\to\infty} S(Q,\omega) = S_{\rm IA}(Q,\omega) = \int_{-\infty}^{+\infty} n(\mathbf{p}) \delta\left[\omega - \frac{Q^2}{2M_{\rm He}} - \frac{\mathbf{Q}\cdot\mathbf{p}}{M_{\rm He}}\right] \frac{d\mathbf{p}}{(2\pi)^3} . \tag{2.6}$$

The δ function in Eq. (2.6) represents the conservation of energy and momentum for the scattering of a neutron from a single atom. In the IA the distance probed by the neutron is much shorter than the typical distance traveled by the scattering helium atom before it is significantly affected by interactions with other atoms. The recoiling atom then acts as a free particle during the collision. For smooth interatomic potentials with Fourier transforms which decrease exponentially with Q, the IA is valid in the $Q\rightarrow\infty$ limit.[39] As a consequence, the IA limit can be reached even if the atom is bound in a confining potential. It fails, however, for a potential with an infinitely repulsive hard core.[40] Since the interatomic forces in helium are steeply repulsive at short distances, one might suspect that very large momentum transfers may be required for the IA to be obeyed.

At high Q, the scattering from an isotropic system such as a liquid no longer depends separately on Q and ω. The dynamic structure factor can be expressed as a function of a single scaling variable Y (Ref. 39)

$$\lim_{Q\rightarrow\infty}(Q/M_{\mathrm{He}})S(Q,\omega)\rightarrow J(Y)\ , \tag{2.7}$$

where

$$Y\equiv(M_{\mathrm{He}}/Q)(\omega-\omega_r) \tag{2.8}$$

is the component of the momentum along the direction of $\mathbf{Q}$, and $J(Y)$ is the longitudinal momentum distribution if $S(Q,\omega)$ satisfies the IA. In the IA, $J(Y)$ is simply related to the momentum distribution

$$\begin{aligned}J_{\mathrm{IA}}(Y)&=2\pi\int_{|Y|}^{+\infty}pn(p)dp\\&=\int_{-\infty}^{+\infty}\int_{-\infty}^{+\infty}n(p_x,p_y,Y)dp_x dp_y\ ,\end{aligned} \tag{2.9}$$

where the direction of $\mathbf{Q}$ is chosen to lie along the z axis. $J_{\mathrm{IA}}(Y)$ exhibits several features which are characteristic of the IA. It is symmetric about $Y=0$ and depends on Q only through the scaling variable Y. These features are equivalent to the more familiar conditions that $S(Q,\omega)$ satisfies in the IA. For $S_{\mathrm{IA}}(Q,\omega)$, the scattering is centered at and is symmetric about the recoil energy ω_r and the width of the scattering is directly proportional to Q and inversely proportional to M_{He}. In liquid helium, both of these conditions are well satisfied for $Q>15$ Å^{-1}.[41] However, Y scaling alone does not necessarily imply the validity of the IA. For atoms with infinitely repulsive hard-core interactions, for example, $S(Q,\omega)$ obeys Y scaling in the $Q\rightarrow\infty$ limit, but the function of Y to which it scales is not the longitudinal momentum distribution.[40]

The IA only approximately describes the scattering for the momentum transfers reached in experiments to date. Deviations from the IA, known as final-state effects, result from the interaction of the recoiling helium atom with its neighbors during the scattering process. These interactions alter the ideal free-particle behavior of the final state of the recoiling atom required for the IA to be obeyed.

In a separate paper, we report a detailed comparison of the various theories for FSE.[42] At the Q's used in this experiment, final-state effects, while certainly present, are simple enough to be amenable to theoretical treatment. We have found that a recent theory by Silver[43] provides an excellent description of FSE in liquid helium in both the normal and superfluid phases at $Q=23$ Å^{-1}. Other theories, while capable of providing a description of FSE in the normal liquid phase which is consistent with the experimental data, do not accurately describe FSE in the superfluid phase.[42] In this paper, we shall restrict our discussion to Silver's theory.

In the first estimate by Hohenberg and Platzman,[26] FSE in helium were calculated within the simple approximation that the struck helium atom scatters from its neighbors at a constant rate proportional to the helium-helium atom cross section and to the atomic density. In fact, this scattering rate is not constant due to the strong spatial correlations which exist among the atoms. Silver's theory for FSE takes into account the effects of the ground-state spatial correlations in the liquid, which cause the width of the FSE broadening function to be narrower than the original estimate of Hohenberg and Platzman. Within Silver's theory, FSE can be expressed as a convolution of a final-state broadening function $R(Y)$ with the IA expression

$$J(Y)=\int_{-\infty}^{+\infty}R(Y-Y')J_{\mathrm{IA}}(Y')dY'\ . \tag{2.10}$$

The second-moment sum rule for incoherent scattering imposes a constraint on the shape of $R(Y)$. Since both $J(Y)$ and $J_{\mathrm{IA}}(Y)$ obey the second-moment sum rule, the second moment of $R(Y)$ must vanish. For this reason, $R(Y)$ must possess negative tails at high Y. As a result, the convolution of a function with $R(Y)$ both broadens the function and also redistributes its intensity in a manner which cannot be viewed as a simple broadening.

We note that within Silver's theory FSE have little effect on the scattering observed in the normal liquid. This is so because the scattering in the normal liquid is broad and nearly Gaussian, and a convolution of $R(Y)$ with a much broader Gaussian will have little effect on its width and, according to the zeroth-moment sum rule, no effect on its total area. However, FSE are important for the relatively narrow non-Gaussian $n(p)$ below T_λ.

The observed scattering, which is proportional to $J(Y)$, provides direct information on the shape of $n(p)$. For example, if $n(p)$ is Gaussian then $J(Y)$ is also a Gaussian with the same second moment. The condensate, which appears as the three-dimensional δ function in $n(p)$, is a one-dimensional δ function in $J(Y)$. However, while there is a direct relationship between the shape of $n(p)$ and the shape of $J(Y)$, it is not a one-to-one correspondence.

To illustrate this fact, consider two recent calculations of the ground state $n(p)$ using variational[18] and GFMC (Ref. 20) techniques and shown in Fig. 1(a). Both calculations predict a condensate fraction, which appears as a δ function with $n_0=9.2\%$. Both calculations also predict quite similar behavior at intermediate and large p. However, they differ markedly at small p. The variational calculation exhibits singular behavior due to coupling of long-wavelength phonons to the condensate which are not present in the GFMC result, presumably due to

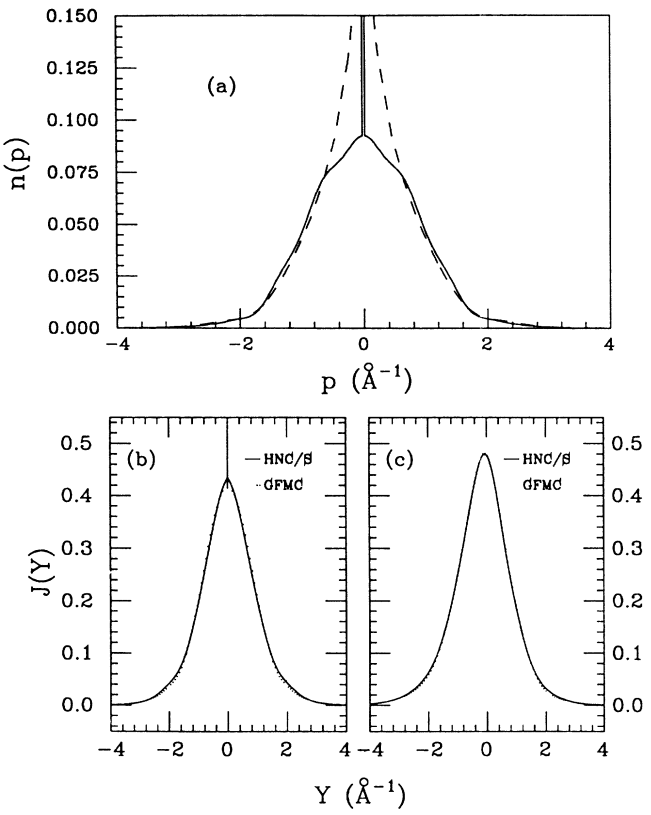

FIG. 1. (a) shows two theoretical calculations of $n(p)$ in liquid helium at $T=0$ K. The solid curve is the GFMC result, and the dashed curve is the HNC/S variational result. (b) shows the longitudinal momentum distributions $J(Y)$ corresponding to the two ground state $n(p)$'s in (a). (c) shows the combined effects of the convolutions of the $J(Y)$'s in (b) with the instrumental resolution function and Silver's final-state broadening function.

finite-size effects in the calculation.

While $n(p)$ for these two calculations is quite different, the corresponding $J_{\mathrm{IA}}(Y)$ is remarkably similar, as shown in Fig. 1(b). The singular behavior, which is the dominant feature in the variational $n(p)$ at small p, is quite small in $J(Y)$. This insensitivity to some of the details of $n(p)$ at small p is a direct consequence of the IA. $J(Y)$ is the momentum distribution in the direction of the momentum transfer, averaged over the longitudinal components, and is proportional to the integral of $pn(p)$. Weakly singular features at small p, such as the condensate-induced singular behavior, will be suppressed due to the p in the integrand. The δ function due to the condensate, of course, is still present in $J(Y)$.

When FSE are taken into account the (now small) differences between the predicted scattering for the two calculations all but disappear, as shown in Fig. 1(c). The predictions of the two very different $n(p)$'s are not nearly indistinguishable. In principle, the differences between the two different $n(p)$'s are still present in Fig. 1(c). In practice, a measurement of the scattering would require fantastically good statistical accuracy to observe these differences.

In principle, we can invert this procedure and obtain $n(p)$ directly from $J(Y)$ using

$$n(p)=\frac{-1}{2\pi Y}\frac{dJ(Y)}{dY} . \tag{2.11}$$

In practice, converting from an experimentally determined $J(Y)$ to $n(p)$ presents several difficulties. First, in order to use Eq. (2.11) the instrumental resolution and final-state effect broadening must be removed. Deconvolution, particularly on data with statistical noise, is an unstable and ill-defined procedure. In addition, numerical differentiation substantially increases the error associated with the data and can only be avoided if the data is smoothed or the results are otherwise biased in some way. Finally, in order to obtain $n(p)$ the differentiated data must be divided by Y, and the results of this division are particularly susceptible to any statistical fluctuations at small Y.

Because of these difficulties, we have chosen not to convert the results of our measurements to $n(p)$. Instead, we first convert the theoretical predictions for the momentum distributions to $J(Y)$. We then convolute the theoretical predictions with both the instrumental resolution function and the FSE broadening function due to Silver and compare the result directly to the data. In this way, the errors in the data due to counting statistics can be used to place meaningful constraints on the shape of the underlying momentum distribution, and all of the problems mentioned above are avoided.

III. EXPERIMENTAL DETAILS

Inelastic neutron scattering measurements of liquid helium were carried out using the PHOENIX spectrometer at the Intense Pulsed Neutron Source (IPNS) at Argonne National Laboratory. IPNS is a spallation source that generates a short burst of neutrons with a usable flux over a wide range of energies. Because IPNS produces a relatively intense flux of high-energy neutrons, measurements at relatively large momentum transfers (20–30 Å^{-1}) are practical.

PHOENIX is a time-of-flight (TOF) spectrometer with a Fermi chopper before the sample to monochromate the pulsed beam from the spallation source. The chopper-source phasing determines the incident energy, which was approximately 500 meV for these measurements. The chopper and sample are 12.55 and 13.6 m from the source, respectively, and the incident beam is 7.5-cm wide and 10-cm high at the sample position. Low-efficiency BF_3 monitors are located 0.68 m before and 2.83 m after the sample to characterize the incident beam. Scattered neutrons are detected using 25 ^{3}He detectors. The cylindrical detectors are 2.5-cm diam and 0.45-m long. As a result of space constraints enforced by the preamplifier electronics, the detectors are staggered to reduce their angular spread. The detectors are located an average distance of 3.8 m from the sample and cover scattering angles between 135° and 145° in a horizontal scattering plane. The details of the instrument will be described more fully elsewhere.[44]

The helium sample was contained in a cylindrical sam-

ple cell made of 6061-T6 aluminum. The cell was 0.10-m high with an inner diameter of 0.04 m and a wall thickness of 1.6 mm. With a total volume of 130 cm^3, the cell contained approximately 5 mol of helium at the densities used for these measurements. The cell was attached to the mixing chamber of a dilution refrigerator in a specially designed cryostat with no cryogens in the neutron beam. Thin (0.05 mm) Al windows in the radiation shields reduced the amount of material in the incident and scattered neutron beam paths. The cell temperature was monitored using germanium resistance thermometers attached to the top and bottom of the cell.

The monitor detectors are used to determine the total flux incident on the sample. They are also used to determine the distribution of the energy and time of arrival of the incident neutron pulse at the sample position. The observed monitor spectra are asymmetric, primarily due to the asymmetric distribution of the time of emission of neutrons from the pulsed source moderator. To extract the mean incident energy and time of arrival the observed monitor spectra are fit to the results of a Monte Carlo simulation of the incident beam. The simulation takes into account the incident pulse spectrum, which has been independently determined,[45] the chopper transmission, and the physical extent of the incident beam. The energy and time of arrival at the sample are recorded for approximately 10^5 neutrons. The means of these distributions are then chosen to represent the average energy and time at sample.

The number of neutrons arriving at the detectors as a function of time of flight is histogrammed individually for each of the detectors. The TOF data is recorded in 2 μsec channels from 300 to 5000 μsec after the initial neutron pulse. The data from each detector is converted to $S(Q,\omega)$ using the time at sample and incident energies obtained from the fits to the monitor spectra discussed above. Finally, the data for each detector is converted to $J(Y)$ using the mean energy and momentum transfer for each point.

Normally, TOF data from several detectors is added together during data collection to increase the statistical accuracy of the measurement at the expense of increasing the instrumental resolution width. In the case of deep-inelastic neutron scattering measurements the position of the peak depends strongly on the momentum transfer, and therefore the scattering angle. For the detector configuration used in PHOENIX this leads to a shift in the peak center of approximately 10 meV across the detector bank. If the data were simply added together, this shift would broaden the observed scattering by this amount.

This undesirable broadening may be eliminated and the statistical accuracy increased by taking into account the scaling properties inherent in deep-inelastic neutron scattering. We take advantage of this scaling behavior by converting the observed scattering to $J(Y)$ before adding the data from each detector together to increase the statistical accuracy. The data from each detector, when converted to $J(Y)$, will have the same peak center and width. The undesirable broadening that results from combining the data from several detectors at the data collection stage is eliminated. Thus, we obtain a significant increase in the statistical accuracy by combining the results of several detectors, but with a resolution effectively determined by the width of a single detector.

The procedure described above implicitly assumes that the data approximately Y scale. As noted in Sec. II, Y scaling behavior has been observed in previous measurements of liquid helium for $Q > 15$ Å^{-1} and is well satisfied at the momentum transfers used in these measurements (23 Å^{-1}). We have also verified this behavior directly with the present results by individually examining the data from each detector. We find that, within the limited statistical accuracy obtainable from a single detector, Y scaling behavior is indeed observed.

The instrumental broadening must also be nearly constant over the detectors combined together for this procedure to be valid. We have verified directly, using a simulation of the instrumental resolution, that the instrumental broadening is fairly constant for the limited range of scattering angles covered by our single detector bank. In addition, our calculations of the instrumental resolution, which will be discussed later, implicitly include any variation in the instrumental broadening across our detector bank.

A complication with this procedure arises since the data, which are recorded as TOF data in evenly spaced time intervals, do not have the same width or starting point when converted to Y due to the differing distances and angles of the detectors. Therefore, the data need to be rebinned to a common Y scale before they can be added together. While the proper absolute size of the errors is maintained in this process, it unavoidably introduces some correlation between the individual points. We choose the new Y scale, to which the data are rebinned, so that it approximately matches the original scale near the peak center. This reduces the undesirable correlation between the data points to a small level.

Data were collected at several temperatures between 0.35 and 4.2 K with a liquid density of 0.147 g/cm^3. Approximately 40 h were required at each temperature to obtain adequate statistics. A typical data set, converted to $J(Y)$ and with the detectors combined to decrease statistical noise, for both the empty cell and the cell containing liquid at $T=2.8$ K is shown in Fig. 2. This data were taken with an incident energy of 496.7 meV. The data shown correspond to a mean momentum transfer at the helium peak of 23 Å^{-1} centered at $Y=0$. The peak centered near $Y=-12$ Å^{-1} is due to the sample cell, radiation shields, and cryostat windows. Note that the helium and aluminum peaks are almost completed separated.

A continuous rise in the scattering intensity is observed with increasing Y. This is due to high-energy neutrons and gammas present in the initial burst from the neutron source that are moderated by the beryllium in the chopper and in the shielding around the instrument. This results in a background scattering that has a nearly exponential decay in TOF. When converted to $J(Y)$ this scattering appears as a background that increases with increasing Y. The contribution of this background is slightly sample dependent since some of the neutrons moderated by the chopper are then scattered by the sam-

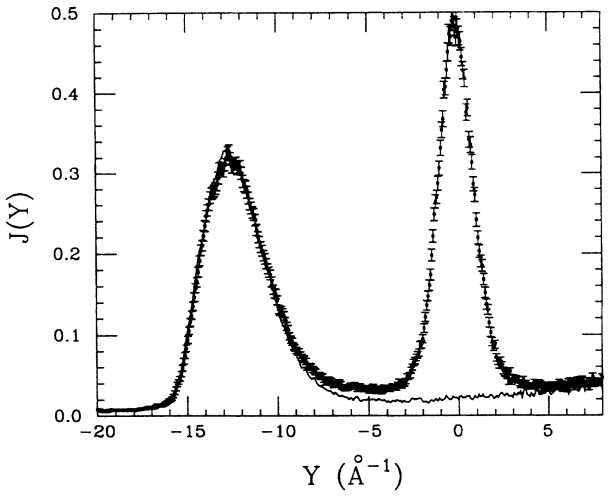

FIG. 2. The points are the scattering at $T=2.8$ K with helium in the cell. The line is the empty-cell data at 4.2 K.

ple. We found that this background was well described by a single exponential decay in TOF. The fitted exponential, which accounts for only a few percent of the intensity in the region of the helium peak, was removed from the raw data before conversion from TOF to $S(Q,\omega)$.

To obtain the scattering due to the liquid alone, the scattering due to the sample cell must be removed. Subtraction of the empty-cell scattering from the scattering with the cell full is carried out after the TOF data has been converted to $J(Y)$. This removes small variations in the phasing between the neutron source and the chopper that slightly shift the incident energy from run to run. These variations result in shifts of the incident energy on the order of 1 meV (less than 0.2%). While these shifts are small, they do result in a sufficient shift of the position of the cell scattering to be observable in the subtractions. Converting to $J(Y)$ before subtracting the cell scattering removes these shifts to the extent that the Q dependence of the empty cell scattering, which is small at these Q's, can be ignored.

Attenuation of the incident beam by the sample must also be taken into account when subtracting the empty-cell scattering. The primary effect is an attenuation of the signal from the rear of the cell due to the scattering of neutrons as they pass through the sample, once in the incident beam and once again in the scattered beam. Correction for these effects has been dealt with adequately in the past for the continuous incident beam from reactor sources. In this case, the effect of beam attenuation simply results in a multiplicative correction to the empty-cell scattering before subtraction.

The situation is more complex for TOF instruments. Due to the time structure in the incident pulse, neutrons scattering from the rear of the cell arrive at the detectors at a different time than neutrons from the front of the cell. Therefore, the additional scattering of the helium not only reduces the cell contribution, but also shifts it in time. We correct for the sample attenuation and this small shift before subtracting the empty-cell scattering using a Monte Carlo simulation of the instrument which is described elsewhere.

After subtraction of the empty-cell signal, a small residual sample-dependent component remains. This component is approximately five times as wide as the helium peak and is due to multiple scattering from the cryostat components. Similar backgrounds have been observed in other inelastic scattering experiments using the LRMECS chopper spectrometer at IPNS.[46] In these experiments the observed background depended upon the sample but was nearly independent of angle from 15° to 110°. Absolute intensity measurements, which are discussed below, also support our identification of this component as multiple scattering from the cryostat. Subsequent modification of the apparatus to remove the possibility of this scattering using neutron-absorbing boron nitride plates essentially eliminated this component. In this work, the contribution from this component is determined by either fitting a broad Gaussian or a linear function to the wings of the scattering. The fit may then be subtracted from the observed helium scattering to remove this component. Removing this broad component, using either technique, does not significantly change the shape of the observed peak.

An absolute intensity scale for the scattering was obtained by measuring a known scatterer, low-density (0.0073 g/cm^3) helium gas at 5.6 K. The measurement was performed using the same experimental setup and cell which were used in the liquid measurements. At this low density, the effects of multiple scattering and sample self-shielding were under 1% and essentially only single helium scattering events were observed. The integrated scattering is then defined to have a unit area so that it satisfies the zeroth-moment sum rule for incoherent scattering. This provides an absolute intensity scale to within the 5% statistical uncertainty in determining the area of the helium peak. This measurement also provides a check on our resolution calculations, which are described below.

The scattering in the liquid is placed on an absolute intensity scale using the helium-gas measurements and the known ratio of the liquid and gas densities. In the liquid sample self-shielding, due to the decrease in intensity of the incident beam as it is scattered by the liquid, is on the order of 10%. The instrument simulation is used to determine the correction for sample self-shielding so that the scattering may be placed on an absolute scale. The contribution of multiple scattering in the bulk liquid was also calculated. At these high Q's, multiple scattering involving the bulk liquid and/or aluminum sample cell makes a negligible contribution to the liquid scattering. Previous calculations of the contribution of multiple scattering in the high-Q limit have drawn the same conclusion.

The effects of instrumental resolution must be taken into account in order to accurately determine the true scattering function. In general, the instrumental broadening is a complicated function depending on the energy and the momentum transfer and the instrument geometry. In addition, for TOF spectrometers using

pulsed sources the instrumental broadening is asymmetric, mainly due to the asymmetric moderator distribution. A simple closed form expression for the resolution function is not possible in general.

A Monte Carlo simulation of the instrument response function is used to correct for instrumental broadening. A model form for the scattering is used as input to the simulation and the resultant scattering, including resolution effects, is calculated for each detector using the incident beam properties obtained from the monitor fits and the known instrument geometry. The output of the simulation, in counts versus time of flight, is in the same form as the experimental data and is processed using the same analysis programs. Any errors in the choice of the mean energy and time at sample will be identical to those in the observed scattering. The resultant resolution broadened $J(Y)$ can then be directly compared to the observed spectra on an absolute scale.

The input of the simulation may be a theoretical calculation of the scattering to be compared with the data or a model scattering function, such as a Gaussian $J(Y)$. The results can be directly compared to the observed scattering and χ^2 evaluated to determine the goodness of fit. In the case of a model scattering function, the parameters of the model can be adjusted to obtain the best agreement, as determined by the smallest χ^2. Errors may be assigned to the model parameters by performing simulations in the neighborhood of the best fit and using the curvature of the χ^2 surface.

We used the procedure described above to compare our observed scattering to theoretical calculations. Fits of a model scattering function could also be carried out using this procedure by continuously adjusting the model parameters and rerunning the simulation. However, this is extremely time consuming. Therefore, it is convenient to express the effects of instrumental resolution as a simple one-dimensional convolution of a broadening function with the model scattering. Unfortunately, this is not generally possible since the resolution is a function of four variables, the energy transfer and the three components of the momentum transfer.

In particular cases an effective resolution function which is a simple one-dimensional convolution can be defined. In terms of this effective resolution function, $I(Y)$, the observed resolution-broadened scattering $J_{\rm obs}(Y)$ is

$$J_{\rm obs}(Y)=\int_{-\infty}^{\infty} I(Y-Y')J(Y')dY' , \tag{3.1}$$

where $J(Y)$ is the unbroadened scattering function. Such a definition will be appropriate when the instrumental broadening does not depend strongly on the details of the scattering function measured. In this case, an effective resolution broadening may be calculated for a scattering function close to the true scattering and used for model functions that do not differ significantly from this shape.

In our case, we use a model scattering function, $J_{\rm model}(Y)$, that closely approximates the observed helium scattering for $J(Y)$. The instrumental simulation is then used to calculate $J_{\rm obs}(Y)$ and $I(Y)$ is obtained by deconvoluting $J(Y)$ from $J_{\rm obs}(Y)$. This yields a broadening function which will accurately represent the instrumental broadening for scattering functions that are similar to $J_{\rm model}(Y)$. To obtain the effective resolution function appropriate to this work we use a Gaussian $n(p)$ and the IA. This provides a model scattering function that is similar to the observed scattering and exhibits the same Q dependence and scaling behavior. Figure 3 shows the effective instrumental resolution obtained using this model for the scattering. The instrumental broadening has a FWHM of ~ 0.6 Å^{-1}, comparable to the resolution used in previous measurements at reactors. The effective resolution was insensitive to the width of the model scattering, for widths ranging from 0.2 to 0.8 Å^{-1}. This range is comparable to the widths observed in these measurements.

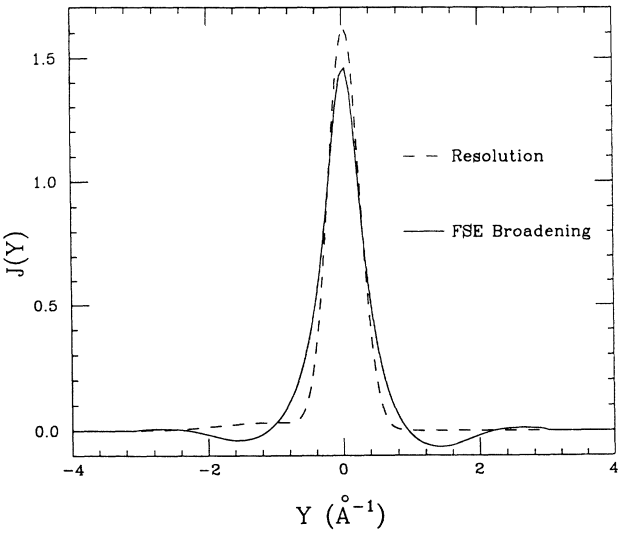

FIG. 3. The solid line is the FSE broadening function due to Silver. The dashed line is the effective instrumental resolution function $I(Y)$ of the PHOENIX spectrometer for the conditions of this experiment.

IV. RESULTS

The scattering was measured from the bulk liquid at temperatures of 0.35, 1.0, 1.5, 1.8, 2.0, 2.3, 2.8, 3.5, and 4.2 K. All of the measurements were carried out at a constant density of 0.147 g/cm^3. The choice to perform the measurements at constant density was made for several reasons. First of all, the momentum distribution at these temperatures and pressures is dominated by the effects of zero-point motion. Zero-point motion, in turn, depends sensitively on the effective volume available for the motion of the atoms, which is directly related to the density.[47] The density is thus the most physically reasonable variable to keep constant in a search for temperature-dependent effects in helium. In addition, many systematic effects whose influence may be imperfectly treated in the data analysis procedure, such as final-state effects, multiple scattering, sample attenuation, and the absolute scattering intensity, are primarily functions of density. By performing the measurements at constant density, we help to insure that the temperature

dependence of the observed scattering directly reflects the temperature dependence of the underlying momentum distribution.

Figure 4 shows the measured scattering, converted to $J(Y)$ as described previously. The scattering has been converted to an absolute intensity scale using the helium-gas measurements. The integrated intensity of the observed scattering, when sample attenuation is taken into account, is unity at all the temperatures, to within the 5% error in the absolute intensity scale provided by the helium-gas measurement. Thus, the observed scattering satisfies the zero-moment sum rule for incoherent scattering, which indicates that all the scattering is observed.

As shown in Fig. 4, the scattering is broad and featureless at all the temperatures studied. At high temperatures near 4 K, $J(Y)$ is nearly Gaussian with a width determined by zero-point motion. As the temperature is lowered toward T_λ, the observed scattering becomes slightly non-Gaussian, with an increase in the scattering at small Y. The significance of this observation is worth noting. If the momentum can be expressed as a coherent superposition of statistically independent normal modes (not necessarily harmonic), then the momentum distribution must be Gaussian as a consequence of the central limit theorem.[48] The observation of non-Gaussian behavior in $J(Y)$ implies that such a decomposition has limited validity even in the normal liquid. Overall, though, there is little temperature dependence of the scattering in the normal liquid phase.

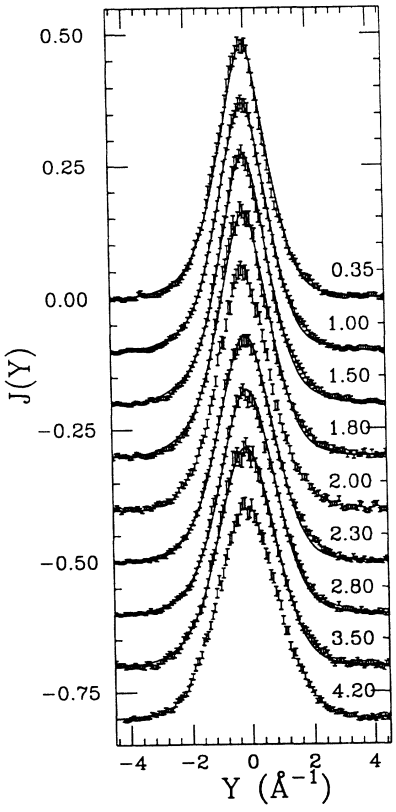

FIG. 4. Observed $J(Y)$ for all the temperatures at a constant density of 0.147 g/cm^3.

A distinct change in the shape of the scattering is observed as the temperature passes from above to below T_λ. The scattering becomes visibly more peaked around $Y=0$ and the shape of the scattering is decidedly non-Gaussian. The intensity at small Y continues to increase with decreasing temperature from 2.0 to 1.5 K, after which the scattering is relatively temperature independent down to the lowest temperature measured. The behavior we observe is similar to the results of previous inelastic neutron scattering experiments at lower Q's. A large change in the scattering is observed at the λ transition, while little change with temperature is observed either above or below the transition.

No sharp feature indicative of a condensate peak is observed in the measurements below T_λ. The data do not provide a direct, theory-independent verification of the existence of a condensate. The general increase in the scattering at small Y is consistent with the development of a condensate peak broadened by instrumental resolution and final-state broadening. However, we note, due to the finite statistical accuracy of the data, the scattering is also consistent with momentum distributions that do not contain a condensate peak. We will discuss this issue in more detail later. At this point, we simply wish to emphasize that we can draw no conclusions regarding the existence or magnitude of the condensate from the observed scattering alone.

A. Comparison to theory

The most direct test of theoretical predictions for $n(p)$ is a direct comparison with the experimental results. Rather than attempt to convert the experimental results to $n(p)$, we instead convert the theoretical predictions to a form that can be compared directly to the experimental results. The IA is used to convert the theoretical $n(p)$ to $J_{\rm IA}(Y)$. Finally, $J_{\rm IA}(Y)$ is broadened by instrumental resolution and, if desired, by FSE.

Figure 5 shows a comparison between the observed

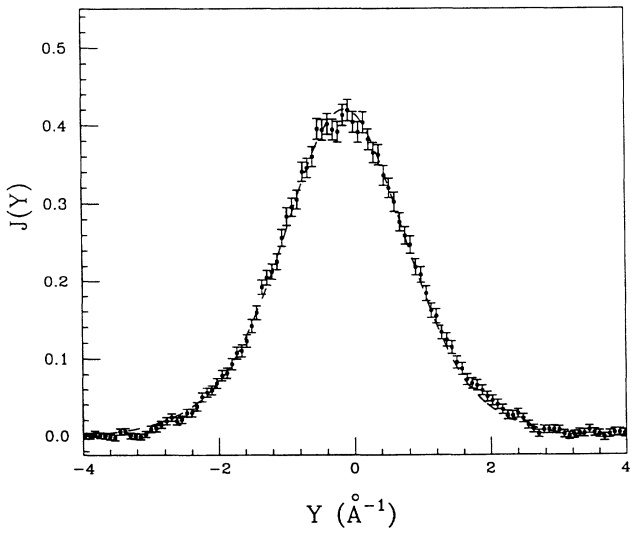

FIG. 5. Observed scattering at $T=3.5$ K. The dashed line is the PIMC prediction of Ceperley and Pollock broadened by the instrumental resolution function only.

scattering in the normal liquid at 3.5 K and a density of 0.147 g/cm^3 and the theoretical prediction of the PIMC results of Ceperley and Pollock[32] at 3.33 K and a slightly lower density of 0.138 g/cm^3. The theoretical prediction has been converted to $J_{IA}(Y)$ using the IA and broadened by the instrumental resolution. No corrections for final-state effects have been made. As described earlier, low-density helium-gas measurements provide an absolute scale for comparison between theory and experiment to within the 5% statistical accuracy of the measurement. Agreement between the theoretical predictions and the experimental observations is obtained despite the neglect of FSE corrections. This is not surprising, since the relatively narrow broadening function should have little effect on the broad, nearly Gaussian $J(Y)$ in the normal liquid.

Figure 6 shows a similar comparison of the experimental results at 0.35 K and the ground-state GFMC calculation of Whitlock and Panoff[20] at the same density. Differences between their prediction and the experimental results are clearly evident. The GFMC calculation predicts substantially higher intensity than the experimental results near the peak center. If final-state effects were absent at our momentum transfers, then one would be forced to conclude that these differences represent a disagreement between theory and experiment, possibly the result of a smaller condensate fraction than predicted by the GFMC calculation. Such a conclusion is unwarranted. Unlike the situation in the normal liquid, FSE must be taken into account to obtain agreement between theory and experiment for the non-Gaussian scattering in the superfluid.

A proper comparison of the theoretical predictions with experiment must include both instrumental resolution *and* final-state effects. Figure 7 shows the comparison between the observed scattering in the normal liquid at 3.5 K and the PIMC calculation broadened by instrumental resolution and convoluted with FSE using Silver's theory. The FSE convolution introduces some slight changes, but they are well within the errors of the observed scattering. Theory and experiment are in agreement for this temperature in the normal fluid.

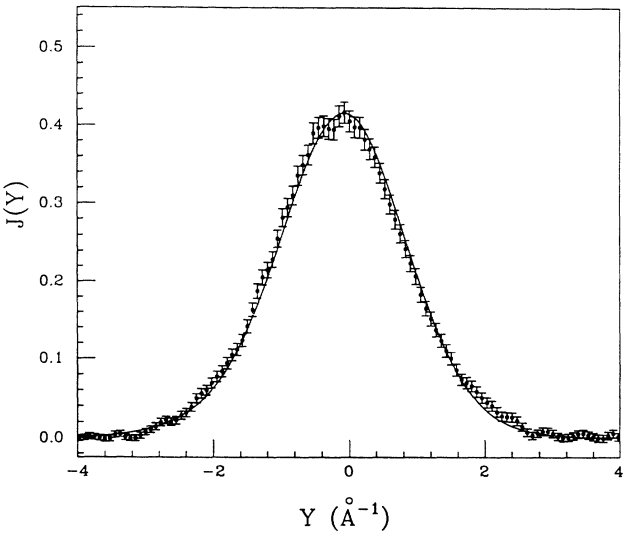

FIG. 7. Observed scattering at $T=3.5$ K. The dashed line is the PIMC prediction of Ceperley and Pollock broadened by the instrumental resolution function and by Silver's FSE broadening function.

Finally, we will take FSE into account in the superfluid phase. The solid line in Fig. 8 is the GFMC prediction, this time with FSE broadening included using Silver's theory. Again, no adjustable parameters have been used. A small (-0.1 Å^{-1}) shift of the simulation relative to the data has been made which is within the uncertainties in the FSE theory. The agreement between theory and

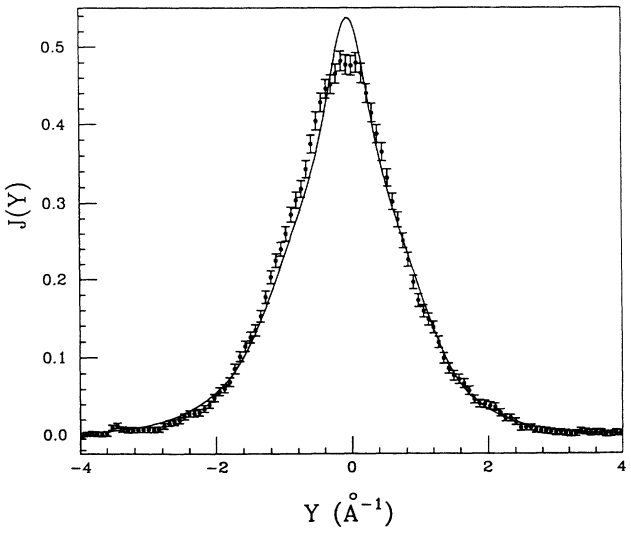

FIG. 6. Observed scattering at $T=0.35$ K. The dashed line is the GFMC prediction of Whitlock and Panoff broadened by the instrumental resolution function only.

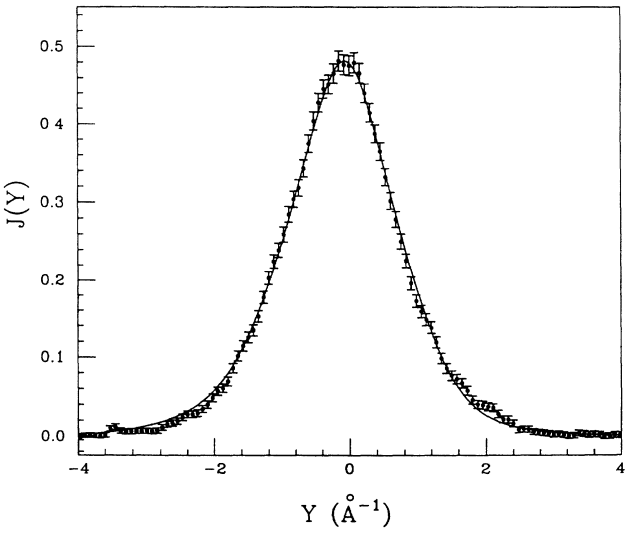

FIG. 8. Observed scattering at $T=0.35$ K. The dashed line is the GFMC prediction of Whitlock and Panoff broadened by the instrumental resolution function and by Silver's FSE broadening function.

experiment is now excellent. For the first time, the theoretical calculations of momentum distributions, FSE theory, and the experimental data are mutually consistent.

The GFMC calculation of the uncondensed component of $n(p)$ in the superfluid can be used to perform an interesting test of the sensitivity of the data to the size of a condensate. Under the assumption that the shape of the uncondensed component of $n(p)$ is given correctly by the GFMC calculation, we can fit the data by using the GFMC calculations for the uncondensed component and replacing the condensate δ function with a Gaussian whose magnitude and width are allowed to vary, subject to the constraint that the normalization of $n(p)$ is maintained. The best agreement is obtained for a Gaussian width of less than 0.05 Å^{-1} and a value for n_0 of 10%. Significant deviations are observed for widths greater than 0.2 Å^{-1} and values of n_0 less than 8% or greater than 12%. The best fit and the two limiting cases are shown in Fig. 9. The data provide clear evidence for a narrow Bose condensate peak with a magnitude of 10±2 %. However, we note that this result depends on the form used for the uncondensed component of $n(p)$. As will be shown later, if a different form for the uncondensed $n(p)$ is chosen, the data is also consistent with no condensate fraction. This value for the condensate fraction and the limits we have placed on it are model dependent.

We have also compared our data at 0.35 K to the HNC/S variational calculations of $n(p)$ extended to $T=0.35$ K by Manousakis and Pandharipande.[18] Figure 10 shows the HNC/S $n(p)$ converted to $J(Y)$, broadened by instrumental resolution, and convoluted with Silver's FSE broadening function along with the experimental data. The agreement between theory and experiment is also excellent for the HNC/S calculation. The fact that good agreement can exist despite the presence of a weak condensate-induced singularity in the variational $n(p)$ was explained earlier in Sec. II.

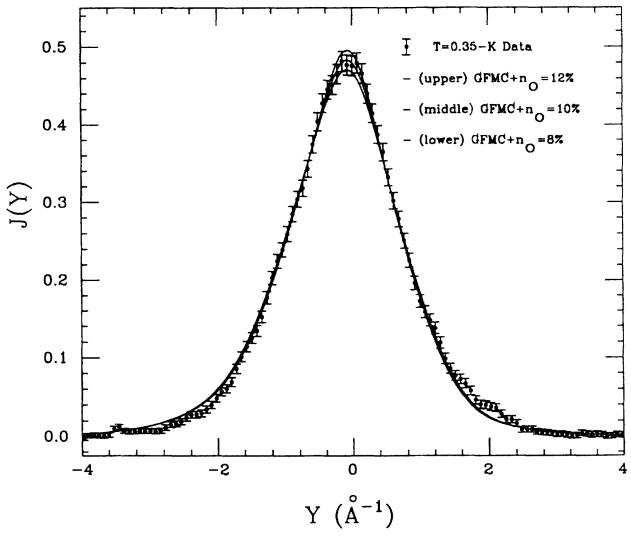

FIG. 9. Observed scattering at $T=0.35$ K. The three fits correspond to the momentum distributions for three different assumed values of the condensate fraction with an uncondensed component of the same shape as the GFMC uncondensed component of Whitlock and Panoff.

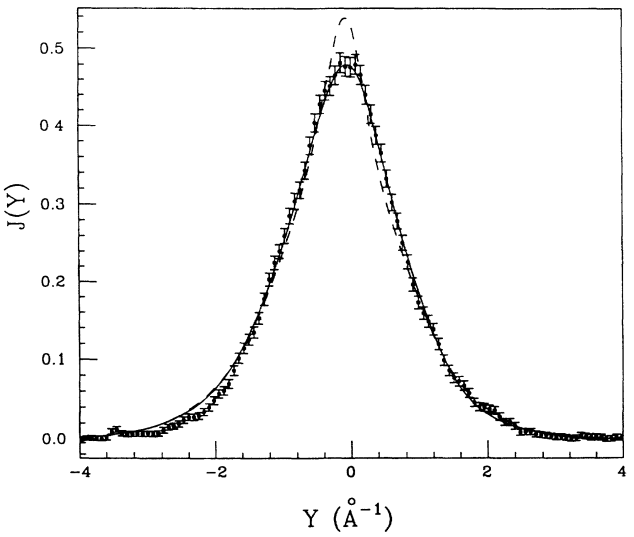

FIG. 10. Observed scattering at $T=0.35$ K. The dashed line is the HNC/S prediction of Manousakis and Pandharipande broadened by the instrumental resolution function only. The solid line is the HNC/S prediction of Manousakis and Pandharipande broadened by the instrumental resolution function and by Silver's FSE broadening function.

There is one feature in the data for which we have no explanation. A small bump superimposed on the tail of the main scattering peak is present near $Y=2$ Å^{-1} which is not visible at $Y=-2$ Å^{-1}. This bump is also present near $Y=2$ Å^{-1} at higher densities in the normal fluid, superfluid, and solid phases for $Q=23$ Å^{-1} and at the density of this paper for lower Q's down to $Q=10$ Å^{-1} in data taken on the PHOENIX spectrometer at IPNS.[49] A similar bump is evident in helium data taken on the High Energy Transfer (HET) spectrometer at the ISIS Neutron Source at Rutherford Appleton Laboratories for $Q=12$ Å^{-1} and 14 Å^{-1}.[50]

This asymmetric feature in the observed scattering cannot be a property of the underlying momentum distribution because the sample container constraints the total momentum of the liquid to vanish. Since the scattering data on the positive Y side of the recoil peak corresponds to the neutrons arriving at the detectors at later times, it might be possible to attribute the asymmetric feature to the effects of multiple scattering, which, if present, would produce an asymmetry in the observed scattering in the same direction. However, the relative size of this asymmetric feature appears to be the same for all of the experiments mentioned above despite the fact that the sample sizes vary by an order of magnitude, with differing sample cell volumes, geometries, and shielding configurations. Since the relative magnitude of a multiple-scattering signal should decrease with a decreasing scattering volume, this explanation for the origin of the bump is made somewhat unlikely. Finally we note that no present theories for FSE predict any such effect. The

asymmetric bump remains an unexplained feature of the inelastic scattering data.

B. Deconvolutions

Direct comparison of the observed scattering to theoretical results is useful for testing the theoretical predictions. However, it only provides information regarding the specific theory compared to the data. It is desirable to obtain a representation of the underlying momentum distribution which is independent of particular theories. This capability is essential for the extraction of model independent values of the kinetic energy and the condensate fraction. In order to implement this goal, both instrumental resolution and final-state broadening must be removed from the observed scattering.

Deconvolution of instrumental broadening from statistically noisy data is an ill-posed problem. For perfect data with no statistical noise, a unique deconvolution is possible. However, when statistical noise is present a whole family of scattering functions can provide an accurate description of the observed scattering. Therefore, any attempt at deconvoluting the broadening must provide some indication of the range of similar curves which also describe the observed scattering.

Rather than attempt to deconvolute the instrumental resolution, we will fit a model function, broadened by resolution and, if desired, by final-state effects, to the observed scattering. We will choose the model such that it has physically realistic behavior and sufficient flexibility to accurately reflect the behavior of the true scattering.

The model scattering function that we have found most convenient for describing the observed scattering is a sum of Gaussians

$$J_{\text{model}}(Y)=\sum_{i=1}^{n}\frac{a_i}{(2\pi\sigma_i^2)^{1/2}}\exp\left[\frac{-(Y-Y_c)^2}{2\sigma_i^2}\right] \quad (4.1)$$

whose amplitudes, widths, and common center may be varied. This form is not unique and many other forms could be used to fit the data. Nevertheless this form, with the restrictions that the amplitudes are always positive and the centers are locked together, does provide a physically realistic model scattering function. It is symmetric and positive definite. It is free of spurious oscillations and other obviously unphysical features which would certainly appear if a direct deconvolution were attempted. In practice, the center of the scattering function Y_c, which relaxes to a value close to the IA result of zero in the course of the fit, is allowed to vary to take into account uncertainties in the center of the FSE broadening function and any errors in the definition of the absolute energy scale.

As an illustration of the range of model scattering functions which can equally well fit the data, consider the three different two-Gaussian fits to the scattering at $T=0.35$ K shown in Fig. 11. The dashed and dotted lines show the underlying distributions which best fit the data if they are constrained to possesses a narrow component by fixing the width of one of the Gaussians to be very narrow ($\sigma=0.03$ in this case). The dashed line has a narrow component with 10% of the total area, and the dotted line has a narrow component with 4% of the total area. Finally, the solid line is a two-Gaussian fit in which both the amplitudes and widths are allowed to vary. The χ^2 values of these fits are very close to each other. If we think of the narrow component of the fits as representing the contribution from the condensate and the broad component as representing the momentum distribution of the uncondensed atoms, then this example shows that, with an appropriate choice for the uncondensed component, the scattering data is consistent with a condensate fraction of zero.

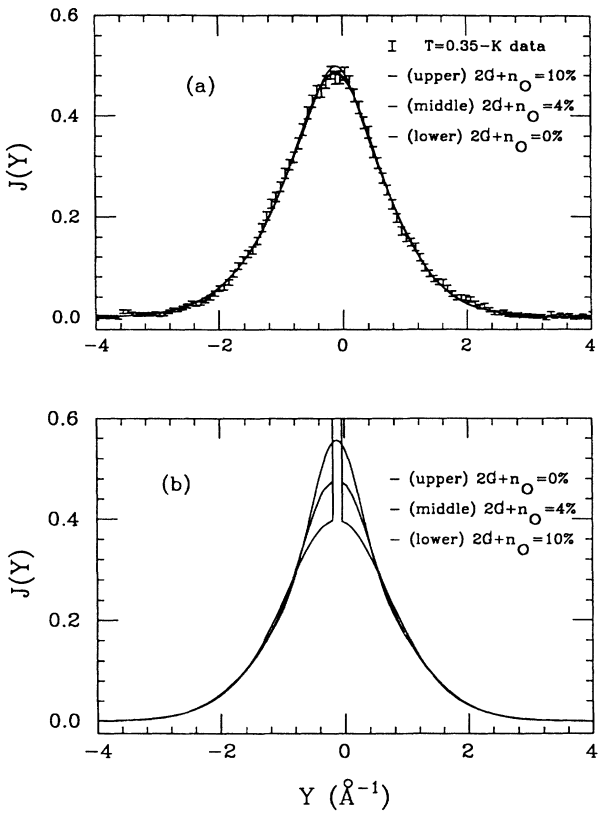

FIG. 11. (a) shows three different two-Gaussian fits to the data at 0.35 K. (b) shows the corresponding model momentum distributions $J_{\text{model}}(Y)$. One is a two-Gaussian fit with a condensate fraction of 10%, another is a two-Gaussian fit with a condensate fraction of 4%, and the third is a two-Gaussian fit with no condensate fraction.

We have performed two-Gaussian fits to the scattering data for all the temperatures both with and without the inclusion of FSE broadening effects. Excellent agreement with the observed scattering can be obtained at all temperatures using only two Gaussians in the model scattering function. The fitted functions are shown in Figs. 12 and 13, and the parameters used are tabulated in Tables I and II. Once again, we emphasize that the particular values of these parameters are only representative of an entire family of values which can equally well characterize the data. The widths and amplitudes of the fitted Gaussians are highly correlated, and a relatively broad

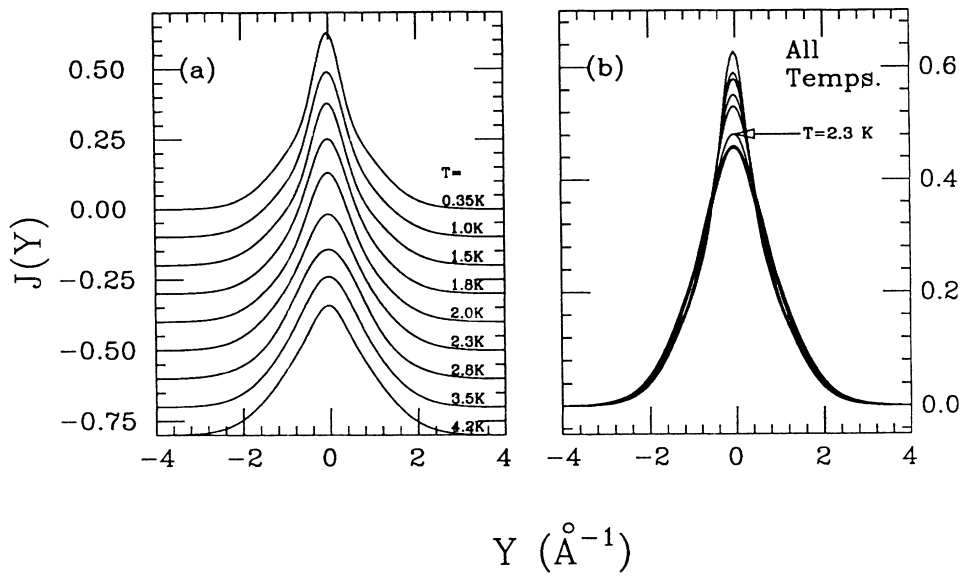

FIG. 12. $J_{\text{model}}(Y)$ for the two-Gaussian fits at all temperatures with instrumental resolution and FSE deconvoluted.

set of parameters can lead to essentially the same shape for the underlying momentum distribution.

The model momentum distributions are important for two reasons. First of all, they reveal the qualitative temperature dependence of the shape of the momentum distribution without the complications introduced by the instrumental resolution and, if Silver's FSE theory is accurate, without complications due to FSE. As can be seen in Figs. 12 and 13, the temperature dependence of the shape of the model momentum distributions is similar to that of the uncorrected scattering data discussed above. They can also be used to obtain model independent values for properties of the momentum distribution such as the average kinetic energy and the condensate fraction. It is true that there is inevitably some model dependence involved in the assumption of a sum of Gaussian functions for the underlying momentum distributions. The fact that the two-Gaussian fits are adequate for all of the temperatures, however, means that any such residual model dependence is too insignificant to be reflected in the information which we can obtain from the scattering data.

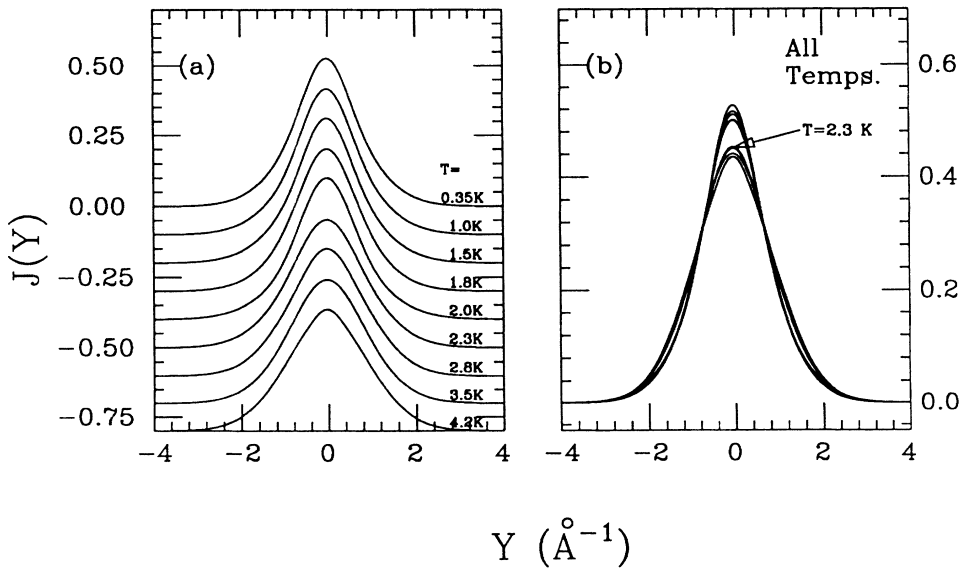

FIG. 13. $J_{\text{model}}(Y)$ for the two-Gaussian fits at all temperatures with only instrumental resolution deconvoluted.

TABLE I. Two-Gaussian fitting parameters, resolution and FSE deconvoluted.

Temp. (K)	A_1 (%)	σ_1 (Å^{-1})	A_2 (%)	σ_2 (Å^{-1})	Y_c (Å^{-1})
0.35	0.785	0.95	0.215	0.29	−0.03
1.0	0.757	0.99	0.242	0.34	−0.02
1.5	0.763	1.00	0.237	0.34	−0.01
1.8	0.765	0.98	0.235	0.39	−0.03
2.0	0.779	1.00	0.221	0.40	−0.04
2.3	0.843	1.01	0.158	0.42	0.00
2.8	0.592	1.11	0.408	0.67	+0.01
3.5	0.875	1.00	0.125	0.45	−0.04
4.2	0.925	1.01	0.075	0.33	−0.03

C. Kinetic energy

The most stringent test of the theoretical calculations of $n(p)$ is, of course, a direct comparison to the experimental results. Another test which can be performed is a comparison of the average kinetic energy per atom, $\langle E_k \rangle$, which the momentum distributions imply. In the incoherent approximation, the kinetic energy is proportional to the second moment of $S(Q,\omega)$. This relation is independent of the validity of Y scaling and the existence of FSE. Given the excellent agreement between theory and experiment for the momentum distributions as shown above, one might naively assume that agreement between the average kinetic-energy values would be automatic. In fact, such an expectation is overly optimistic.

We have used the second-moment sum rule in the form which it assumes in Y space

$$\langle E_k \rangle = \int_0^\infty J(Y) \frac{3\hbar^2 Y^2}{2M_{\mathrm{He}}} dY \tag{4.2}$$

to calculate the $\langle E_k \rangle$ from our two-Gaussian model scattering functions. The observed kinetic energies (Table III) show relatively little temperature dependence below T_λ, ranging from 13.3 K at $T=0.35$ K to 14.8 K at 2.0 K. $\langle E_k \rangle$ jumps to 16.1 K at $T=2.3$ K and increases slowly to 17.1 K at $T=4.2$ K. The size of the kinetic-energy decrease from just above T_λ to the lowest-temperature value is much larger than one would expect using simple models for $n(p)$ in which the uncondensed component is simply reduced in size without changing shape when the condensate appears. Apart from the jump in $\langle E_k \rangle$ across the λ transition, the temperature dependence of $\langle E_k \rangle$ at constant density is smooth.

Above 1 K, the experimental $\langle E_k \rangle$ is slightly lower than, but in fair agreement with, the PIMC calculations. The values for the $\langle E_k \rangle$ from the two-Gaussian models at 1.0–2.0 K range from 14.0 to 14.8 K. These values are in excellent agreement with the PIMC values which range from 14.2 to 14.7 K for temperatures between 1.18 and 1.82 K. Above T_λ, the agreement is also quite good between the two-Gaussian values for the kinetic energy and the PIMC values. In contrast, the experimental $\langle E_k \rangle$ at 0.35 K is 13.3±1.3 K, which is significantly below the GFMC and HNC/S values of 14.3 and 14.9 K, respectively. Despite the excellent agreement obtained for the momentum distribution at 0.35 K, the theoretical and experimental $\langle E_k \rangle$ are different.

The origin of this difference can be exhibited by calculating the $\langle E_k \rangle$ from the second moment as a function of a cutoff momentum Y_c

$$\langle E_k(Y_c) \rangle = \int_0^{Y_c} J(Y) \frac{3\hbar^2 Y^2}{2M_{\mathrm{He}}} dY \ . \tag{4.3}$$

As can be seen in Fig. 14, the experimental and theoreti-

TABLE II. Two-Gaussian fitting parameters, only resolution deconvoluted.

Temp. (K)	A_1 (%)	σ_1 (Å^{-1})	A_2 (%)	σ_2 (Å^{-1})	Y_c (Å^{-1})
0.35	0.718	0.95	0.277	0.49	−0.10
1.0	0.666	1.01	0.331	0.52	−0.09
1.5	0.693	1.01	0.303	0.51	−0.08
1.8	0.675	0.99	0.321	0.56	−0.10
2.0	0.625	1.06	0.369	0.56	−0.08
2.3	0.788	1.01	0.210	0.59	−0.08
2.8	0.909	0.96	0.085	0.46	−0.06
3.5	0.841	0.99	0.157	0.61	−0.11
4.2	0.972	0.97	0.024	0.28	−0.11

TABLE III. Theoretical and experimental kinetic energies.

Temp. (K)	Density (g/cm^3)	$\langle E_k \rangle$ (K/atom)	Error (K/atom)	Source	Method
0.35	0.147	13.3	±1.3	Present	Inelastic
1.0	0.147	14.1	±1.4	Present	Inelastic
1.5	0.147	14.5	±1.4	Present	Inelastic
1.8	0.147	14.0	±1.4	Present	Inelastic
2.0	0.147	14.8	±1.5	Present	Inelastic
2.3	0.147	16.1	±1.6	Present	Inelastic
2.8	0.147	16.6	±1.7	Present	Inelastic
3.5	0.147	16.2	±1.6	Present	Inelastic
4.2	0.147	17.1	±1.7	Present	Inelastic
0.0	0.146	14.9		Ref. 18	HNC/S
0.0	0.146	14.3	±1.0	Ref. 20	GFMC
1.18	0.146	14.2		Ref. 21	PIMC
1.54	0.146	14.4		Ref. 21	PIMC
1.82	0.146	14.7		Ref. 21	PIMC
2.22	0.147	15.9		Ref. 21	PIMC
2.50	0.146	15.9		Ref. 21	PIMC
3.33	0.138	16.0		Ref. 21	PIMC
4.00	0.128	15.6		Ref. 21	PIMC
0.0	0.146	13.7		Ref. 53	Elastic
1.5	0.146	13.8		Ref. 53	Elastic
2.0	0.146	14.3		Ref. 53	Elastic
2.1	0.147	14.8		Ref. 53	Elastic
2.2	0.147	15.8		Ref. 53	Elastic
3.5	0.137	15.8		Ref. 53	Elastic
3.5	0.137	15.3		Ref. 53	Elastic
1.3	0.146	13.4	±0.5	Ref. 50	Inelastic
2.0	0.147	14.5	±0.5	Ref. 50	Inelastic
2.3	0.147	16.5	±0.5	Ref. 50	Inelastic
2.6	0.146	14.9	±0.5	Ref. 50	Inelastic
3.2	0.141	14.8	±0.5	Ref. 50	Inelastic
3.8	0.133	15.8	±0.5	Ref. 50	Inelastic
4.2	0.125	15.7	±0.5	Ref. 50	Inelastic
1.2	0.146	13.2		Ref. 51	Inelastic
4.2	0.146	16.9		Ref. 51	Inelastic
1.1	0.146	13.3		Ref. 52	Inelastic
4.2	0.125	13.6		Ref. 52	Inelastic

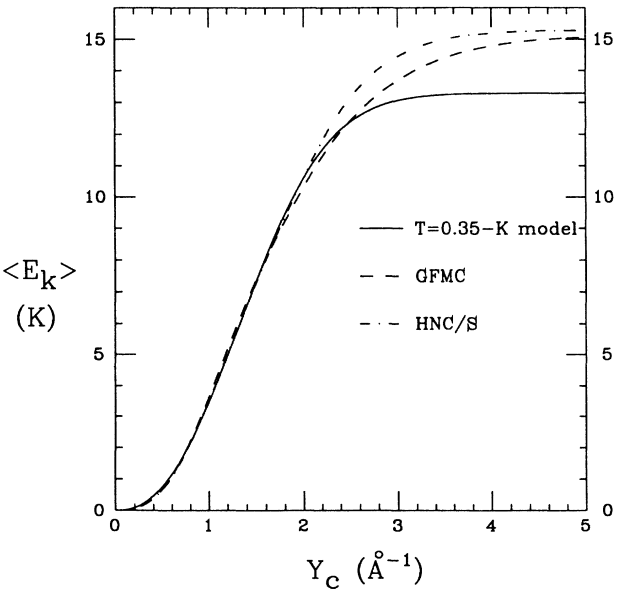

FIG. 14. $\langle E_k \rangle (Y_c)$ vs Y_c at $T=0.35$ K for the GFMC, HNC/S, and model momentum distributions.

cal $\langle E_k(Y_c) \rangle$ are identical up to $Y_c = 2$ Å^{-1}, and the entire difference in the $\langle E_k \rangle$ values comes from the larger momenta in the tails of the distribution. But this is the very region in which the observed scattering is small and the errors due to counting statistics are significant. Since the $\langle E_k \rangle$ is proportional to the second moment, even a small difference in the high-Y tails of the scattering can lead to a large difference in the kinetic energy. The difference in the $\langle E_k \rangle$ can easily be accounted for by assuming a small amount of additional intensity in the poorly known tails of the scattering.

Earlier inelastic scattering measurements at standard volume and pressure[51–53] have also determined the $\langle E_k \rangle$ from the second moment of the scattering. These values have been summarized by Sears[54] and are shown in Fig. 15. The results show little temperature dependence below the λ transition and are in good agreement with our work.

The average kinetic energy has also been determined using neutron or x-ray structure-factor measurements in combination with heat-capacity measurements.[54] The kinetic energy is the difference between the total energy as

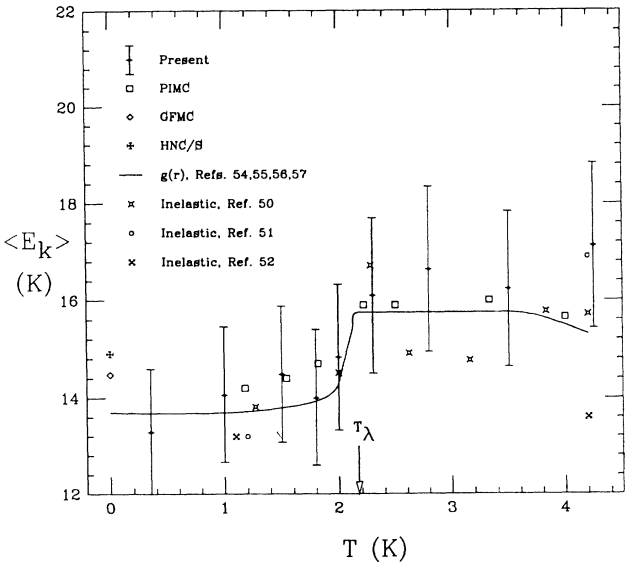

FIG. 15. Compilation of $\langle E_k \rangle$ vs temperature from a variety of measurements. The points with error bars are the results of the present measurements.

determined from the heat-capacity measurements and the average potential energy as calculated using $g(r)$ and the interatomic potential. The average result of the neutron and x-ray values[55–58] is the solid line in Fig. 15. The curve is in good agreement with the present values.

D. Estimate of the condensate fraction

Because of the importance of the presence of a condensate in our present understanding of superfluidity in bulk ^{4}He, several attempts have been made to estimate its size.[27,53,59,60] Given the lack of a detailed microscopic theory for liquid ^{4}He, the only measurable property of the liquid which can unambiguously reveal the size of the condensate is the momentum distribution. Yet no distinct condensate peak characteristic of the superfluid has ever been observed in any deep-inelastic neutron scattering experiment to date. Unfortunately, even the best present method of estimation of the condensate fraction, known as the Sears method,[27] relies on assumptions about aspects of the momentum distribution which are difficult to verify.

We have chosen not to include a discussion on the estimation of the size of the condensate fraction in this paper for two reasons. A detailed discussion of the Sears method, including both a clear indication of the various assumptions involved and a history of its application in the past, would require a relatively large amount of space to be devoted to a method whose physical significance is not compelling. In addition, we are currently developing an alternative method for the estimation of the condensate fraction which may represent a significant improvement on the Sears method. A separate paper on the extraction of the condensate fraction which contains a discussion of both methods is in preparation.[61]

V. CONCLUSIONS

We have shown that excellent agreement exists between the theoretical results and the experimental observations for all aspects of the momentum distribution in liquid ^{4}He. Our results, due to finite instrumental resolution and statistical accuracy, can be described by a range of momentum distributions and a unique determination of $n(p)$ is not possible. In particular, it is possible to obtain agreement with the results in the superfluid both with momentum distributions that contain a condensate contribution and with those that do not. However, the excellent agreement between theory, which predicts a Bose condensate containing $\sim 9\%$ of the atoms near $T=0$, and experiment provide convincing evidence for the existence of Bose condensate. Thus, we believe that these measurements settle beyond any reasonable doubt the long-standing question regarding the existence and magnitude of a Bose condensate in the superfluid.

This recent convergence of theory and experiment has been made possible through several simultaneous advances. The availability of more powerful computational techniques and facilities for the calculation of $n(p)$ has lead to very accurate theoretical predictions. In addition, the development of accurate theoretical predictions for final-state effects, particularly in the superfluid, has allowed *ab initio* comparisons of the theoretical and experimental results. The development of spallation neutron sources has enabled us to obtain high quality, interpretable experimental results with good statistical accuracy.

A better understanding of the strengths and weaknesses of deep-inelastic neutron scattering as applied to determinations of $n(p)$ in quantum systems has also evolved. The insensitivity of the observed scattering to some of the singular behavior in $n(p)$ is now understood, and the difficulties involved in determining the behavior of $n(p)$ for large p are now appreciated. We have tried to indicate which aspects of the momentum distribution are tightly constrained by the measurements and which aspects are not.

Some may be disappointed that the original goal for much of the high-Q neutron scattering work in liquid helium, a direct observation of the condensate peak, has not come to pass. In the foreseeable future, it is unlikely that this goal will be reached in deep-inelastic neutron scattering experiments. But the failure to directly observe a condensate peak is more than offset by the progress in both theory and experiment which has followed from the search. The insights gained from the final-state-effect theories, for example, are applicable to inelastic scattering experiments in other areas of physics. In addition, the numerical and variational calculations which have been successfully tested on helium promise to improve our understanding of many other dense, strongly interacting systems. Finally, the techniques developed in deep-inelastic neutron scattering hold promise for future measurements in liquid ^{4}He at higher densities, liquid ^{3}He, liquid ^{3}He-^{4}He mixtures, ^{4}He in confined geometries, and solid helium. Far from being a disappointment and a curse, the invisibility of the condensate has been a blessing in disguise.

ACKNOWLEDGMENTS

It is a pleasure to acknowledge many enlightening discussions with Dr. J. M. Carpenter and Dr. R. N. Silver. This work was supported by the National Science Foundation through Grant No. DMR-8704288 and by the Department of Energy through the Office of Basic Energy Science, Division of Materials Research support of the Intense Pulsed Neutron Source at Argonne National Laboratory under U. S. Department of Energy Grant No. W-31-109-ENG-38. T. R. S. and W. M. S. acknowledge the support of the Division of Educational Programs at Argonne National Laboratory.

---

*Present address: Biophysics Division, Los Alamos National Laboratory, Los Alamos, NM 87545.

†Permanent address: Lyman Laboratory of Physics, Harvard University, Cambridge, MA 02138.

[1]P. Nozières and D. Pines, *The Theory of Quantum Liquids* (Addison-Wesley, Reading, Mass., 1989), Vol. II, Chap. 6.

[2]A. Griffin, Can. J. Phys. **65**, 1368 (1987).

[3]J. Gavoret and P. Nozières, Ann. Phys. (N.Y.) **28**, 349 (1964).

[4]W. L. McMillan, Phys. Rev. **138**, A442 (1965).

[5]R. A. Aziz, V. P. S. Nain, J. S. Carley, W. L. Taylor, and G. T. McConville, J. Chem. Phys. **70**, 4330 (1979).

[6]D. Schiff and L. Verlett, Phys. Rev. **160**, 208 (1967).

[7]W. P. Francis, G. V. Chester, and L. Reatoo, Phys. Rev. A **1**, 86 (1970).

[8]M. A. Pokrant, Phys. Rev. A **6**, 1588 (1972).

[9]M. L. Ristig, P. M. Lam, and J. W. Clark, Phys. Lett. **55A**, 101 (1975).

[10]P. M. Lam and M. L. Ristig, Phys. Rev. B **20**, 1960 (1979).

[11]Q. N. Usmani, S. Fantoni, and V. R. Pandharipande, Phys. Rev. B **26**, 6123 (1982).

[12]Q. N. Usmani, B. Friedman, and V. R. Pandharipande, Phys. Rev. B **27**, 4502 (1982).

[13]K. E. Kurter and J. W. Clark, Phys. Rev. B **30**, 1342 (1984).

[14]E. Manousakis and V. R. Pandharipande, Phys. Rev. B **30**, 5062 (1984).

[15]M. Puoskari and A. Kallio, Phys. Rev. B **30**, 152 (1984).

[16]C. E. Campbell, K. E. Kurten, M. L. Ristig, and G. Senger, Phys. Rev. B **30**, 3728 (1984).

[17]S. Vitiello, K. Runge, and M. H. Kalos, Phys. Rev. Lett. **60**, 1970 (1988).

[18]E. Manousakis, V. R. Pandharipande, and Q. N. Usmani, Phys. Rev. B **31**, 7022 (1985); E. Manousakis and V. R. Pandharipande, *ibid.* **31**, 7029 (1985).

[19]R. P. Feynman and M. Cohen, Phys. Rev. **102**, 1189 (1956).

[20]P. A. Whitlock and R. Panoff, Can. J. Phys. **65**, 1409 (1987).

[21]P. E. Sokol, R. N. Silve, and J. W. Clark, in *Momentum Distributions,* edited by R. N. Silver and P. E. Sokol (Plenum, New York, 1989), pp. 1–35.

[22]D. M. Ceperley and E. L. Pollock, Can. J. Phys. **65**, 1416 (1987).

[23]R. P. Feynman, *Statistical Mechanics* (Benjamin, New York, 1972), Chap. 3.

[24]E. Manousakis and V. R. Pandharipande, Phys. Rev. B **31**, 7029 (1985).

[25]E. L. Pollock and D. M. Ceperley, Phys. Rev. B **36**, 8343 (1987).

[26]P. C. Hohenberg and P. M. Platzman, Phys. Rev. **152**, 198 (1966).

[27]V. F. Sears, E. C. Svensson, P. Martel, and A. D. B. Woods, Phys. Rev. Lett. **49**, 279 (1982).

[28]H. A. Mook, Phys. Rev. Lett. **51**, 1454 (1983).

[29]S. Ikeda and N. Watanabe, Phys. Lett. A **121**, 34 (1987).

[30]R. S. Holt, L. M. Needham, and M. P. Paoli, Phys. Lett. A **126**, 373 (1989).

[31]M. H. Kalos, M. A. Lee, P. A. Whitlock, and G. V. Chester, Phys. Rev. B **24**, 115 (1981).

[32]P. A. Whitlock and R. N. Panoff, Los Alamos National Laboratory Report No. LA-10227-Z, 1984.

[33]P. Martel, E. C. Svensson, A. D. B. Woods, V. F. Sears, and R. A. Cowley, J. Low Temp. Phys. **23**, 285 (1976).

[34]D. B. Day *et al.*, Phys. Rev. Lett. **59**, 427 (1987); I. Sick, in *Progress In Particle and Nuclear Physics,* edited by A. Faessler (Pergamon, New York, 1985), Vol. 13, p. 165.

[35]V. F. Sears, *Neutron Optics* (Oxford University Press, New York, 1989), Chap. 2.

[36]S. W. Lovesey, *Theory of Neutron Scattering from Condensed Matter* (Oxford University Press, Oxford, 1984), Vol. I, Chap. 3.

[37]H. R. Glyde and E. C. Svensson, in *Methods of Experimental Physics,* edited by K. Sköld and D. L. Price (Academic, New York, 1987), Vol. 23, Chap. 13, p. 303.

[38]A. Rahman, K. S. Singwi, and A. Sjölander, Phys. Rev. **126**, 986 (1962).

[39]G. B. West, Phys. Rep. **18C**, 263 (1975).

[40]J. J. Weinstein and J. W. Negele, Phys. Rev. Lett. **49**, 1016 (1982).

[41]P. E. Sokol, Can. J. Phys. **65**, 1393 (1987).

[42]P. E. Sokol, R. N. Silver, T. R. Sosnick, and W. M. Snow (unpublished).

[43]R. N. Silver, in *Proceedings of the 11th International Workshop on Condensed Matter Theories, Oulu, Finland,* edited by J. S. Arponen, R. F. Bishop, and M. Manninen (Plenum, New York, 1987), Vol. 3, p. 131; Phys. Rev. B **37**, 3794 (1988); **38**, 2283 (1988); **39**, 4022 (1989).

[44]P. E. Sokol *et al.* (unpublished).

[45]S. Ikeda and J. M. Carpenter, Nucl. Instrum. Methods A **239**, 536 (1985).

[46]K. W. Herwig (private communication).

[47]K. W. Herwig, P. E. Sokol, T. R. Sosnick, W. M. Snow, and R. C. Blasdell, Phys. Rev. B **41**, 103 (1990).

[48]V. F. Sears, Can. J. Phys. **63**, 68 (1985).

[49]K. W. Herwig (private communication); R. C. Blasdell and R. O. Simmons (private communication).

[50]W. G. Stirling, L. K. H. Anderson, A. D. Taylor, I. Bailey, and Z. A. Bowden, ISIS Experimental Report No. ULS 85/1RB610, 1989.

[51]O. K. Harling, Phys. Rev. A **3**, 1073 (1971); A. G. Gibbs and O. K. Harling, *ibid.* **7**, 1748 (1973).

[52]H. A. Mook, Phys. Rev. Lett. **32**, 1167 (1974).

[53]A. D. B. Woods and V. F. Sears, Phys. Rev. Lett. **39**, 415

(1977).
[54]V. F. Sears, Phys. Rev. B **28**, 5109 (1983).
[55]H. N. Robkoff and R. B. Hallock, Phys. Rev. B **24**, 159 (1981).
[56]V. F. Sears and E. C. Svensson, Phys. Rev. Lett. **43**, 2009 (1979).
[57]V. F. Sears and E. C. Svensson, Int. J. Quantum Chem. Symp. **14**, 715 (1980).
[58]V. F. Sears, E. C. Svensson, and A. F. Murray (unpublished).
[59]R. A. Cowley and A. D. B. Woods, Phys. Rev. Lett. **21**, 787 (1968).
[60]H. A. Mook, R. Scherm, and M. K. Wilkinson, Phys. Rev. A **6**, 2268 (1972).
[61]W. M. Snow and P. E. Sokol (unpublished).